Journal of Theoretical and Applied Information Technology
15th February 2026. Vol.104. No.3

ISSN: 1992-8645 www.jatit.org E-ISSN: 1817-3195

VESSEL LOOP STRUCTURE-AWARE MULTI-GRADE DIABETIC RETINOPATHY CLASSIFICATION USING ENHANCED TCLLKEN

JAGADEESH VUTLA[1], VISALAKSHI ANNEPU[2]

[1] School of Comuter Science and Engineering, Research Scholar, VIT-AP University,Amaravati,Andhra Pradesh 522237,India
[2] School of Computer science and Engineering,Assistant Professor Senior Grade-1, VIT-AP University,Amaravati,A.P,India.

E-mail : [1] Jagadeesh.23phd7131@vitap.ac.in, [2] visalakshi.a@vitap.ac.in

ABSTRACT

In order to prevent individuals from blindness and blurred vision, timely and accurate Diabetic Retinopathy (DR) diagnosis is essential in the context of the medical field. Therefore, numerous studies have been implemented by a variety of researchers to classify DR using Artificial Intelligence (AI) algorithms and Retinal Fundus Images (RFIs). The fundamental biomarker for recognizing the DR is the vessel loop. However, the conventional works failed to concentrate on investigating the Vessel Loop Structure (VLS) during DR classification, thereby causing poor DR grading. Thus, to upgrade the diagnosis reliability, a significant VLS-aware multi-grade DR classification framework is pivotal. Therefore, This work is driven by the need to develop a more accurate, VLS-aware multi-grade DR classification method using Transfer Complementary Log-Log Karplus-EfficientNet (TCLLKEN). Primarily, the eye-retinal images are gathered and further pre-processed, followed by gray-scale conversion. After that, regions in the gray-scale images are grouped. In the meantime, from the pre-processed images, the Green Channel (GC) is extracted. Subsequently, vessel structure segmentation, vessel graph construction, and VLS extraction are carried out. Lastly, the extracted features, extracted VLS, and pre-processed images are inputted into the proposed TCLLKEN that classifies the multi-grades of the DR efficiently. Overall, through the inclusion of VLS analysis, DR grading accuracy is significantly enhanced across all stages. Hence, highly accurate multi-grade DR classification is achieved by the proposed VLS-aware TCLLKEN model with an accuracy of 98.99%, thus performing better than existing methods.

Keywords: *Diabetic Retinopathy (DR), Blood Vessels (BV), Vessel Loop Structure (VLS), Retinal Lesions (RL), Deep Learning (DL), Proliferative Diabetic Retinopathy (PDR), and Retinal Fundus Images (RFI).*

1. INTRODUCTION

DR, which affects the retina (light-sensitive tissue at the back of the eye), is a major diabetes-related eye complication (Adriman et al., 2021). The individual affected by DR may face several symptoms, including distorted vision, faded colors, dark spots, blindness, and difficulty with night vision, due to the high blood pressure and long-standing diabetes (Sawant & Vibhute, 2025). The tiny blood vessels in the retina are damaged by the increased blood sugar levels, resulting in abnormal vessel growth and lesion formation (Hayati et al., 2023). Further, microaneurysms, soft exudates, hard exudates, and hemorrhages are the common eye retinal lesions (Abbood et al., 2022).

Therefore, timely and accurate diagnosis of DR helps to preserve vision and prevent blindness (Romero-Oraá et al., 2024). In basic terms, the DR is classified into 2 stages, namely Non-Proliferative Diabetic Retinopathy (NPDR) (early stage) and Proliferative Diabetic Retinopathy (PDR) (advanced stage) (Ali et al., 2023). The processes like data collection, pre-processing, feature extraction, and disease classification are encompassed in an automated DR classification (Das et al., 2022). For the early detection and monitoring of DR, Retinal Fundus (RF) images have been widely adopted over the last few decades (Bilal et al., 2021). By utilizing the fundus camera that reveals the retina's blood vessels and structures, RF images are captured (Uppamma & Bhattacharya, 2023), thereby supporting DR

diagnosis. AI (Ikram et al., 2024), including Deep Learning (DL), has gained immense popularity among most of the researchers and Ophthalmologists in the context of automatic RF-based DR detection (Sangeetha et al., 2023). To classify the types of DR, existing approaches utilized machine learning algorithms like support vector machine, random forest, and naïve bayes (Singh et al., 2024). The prior studies used the DL algorithms, such as Convolutional Neural Network (CNN), Visual Geometry Group (VGG), Residual Network (ResNet) (Abini & Priya, 2023), and Deep Neural Network (DNN), to automatically detect and classify DR from RFIs (Meruva et al., 2022). Nevertheless, conventional methodologies struggled to capture the retinal lesions' crucial symptoms.

Conventional algorithms utilized pixel-based segmentation approaches like K-means and Fuzzy C-Means (FCM) to highlight the significant properties of the retinal lesions (Bilal et al., 2022). Many traditional works primarily concentrated on retinal lesions (microaneurysms, hemorrhages, and exudates) and basic vessel segmentation. However, in the prevailing studies, the topological characteristics of retinal vasculature, specifically the VLS, were overlooked. Detailed insight into vascular abnormalities associated with disease progression and severity levels is offered by VLS. The crucial biomarker for recognizing the DR is the vessel loop. Due to the transition from early-stage DR (NPDR) to PDR, vessel loops are formed. The traditional frameworks had poor robustness and accuracy in DR grading owing to the absence of VLS analysis. Therefore, to improve the reliability of the DR prediction outcomes, early DR classification with VLS analysis is essential. Hence, The need to develop a novel framework known as the multi-grade DR classification approach that integrates VLS analysis by using an improved TCLLKEN is what spurred this study. Detailed insight into vessel loop count, loop area, and loop density, which are related to disease progression, is significantly offered by the inclusion of VLS analysis. The proposed work obtains diagnostic accuracy of the DR classification by capturing the disease progression-related factors. Overall, a unique contribution towards more accurate multi-grade DR classification is offered by the proposed work.

1.1 Novel contribution

In the proposed work, a novel scheme named VLS analysis is integrated for DR classification, thus facilitating more reliable and fine-grained multi-grade DR classification. Moreover, to effectively isolate the vessel structures from the retinal tissues, the proposed work carries out the GC extraction, improving the efficiency of the proposed work. Here, to perform vessel graph construction, an improved Minimum Kepler Spanning Tree (MKST) is used, thereby capturing the subtle vessel changes associated with the disease's severity.

1.2 Problem statement

The existing studies have some major drawbacks, which are given as follows,

- None of the traditional methods concentrated on examining the VLS during DR detection, thus leading to poor DR grading and reducing the model's efficiency.
- Due to retinal blood vessels' structural resemblance between vessels and surrounding retinal tissues, the prevailing DR detection scheme (Xu et al., 2024) struggled to separate them. Other retinal tissues, such as microaneurysms, hemorrhages, and neovascularization, shared similar visual properties with blood vessels.
- The conventional work (Usman et al., 2023) was less adaptable to handle patients with varying vessel patterns and lesion appearances.
- The conventional work (Dayana & Emmanuel, 2022) didn't efficiently capture the fine structural and spatial features of retinal patterns, depicting inappropriate DR's diagnosis outcomes.
- The majority of the prior schemes had incorrect DR estimation owing to the low-resolution Fundus Images (FIs), thereby hindering the detection of subtle vascular patterns (thin vessels).
- Some conventional works heavily concentrated on binary classification, which signified the presence or absence of DR instead of categorizing several stages of DR, thus impacting the model's resilience.

1.3 Objectives

The research methodology's fundamental goals are provided below,

- A novel MKST is established to construct the vessel graph structure from the segmented vessels, thereby capturing the VLS, including loop degree, loop area, and loop count. So, the model's prediction capability and trustworthiness are upgraded.

- In the proposed work, GC extraction is carried out to accurately differentiate the vessel thin structures from the surrounding retinal tissues.

- The proposed TCLLKEN integrates Transfer Learning (TL) to effectively handle patients with diverse lesion appearances and vessel patterns.

- The research methodology carries out precise region grouping using the proposed Density Prony-Based Spatial Probability Clustering of Applications with Noise (DPBSPCAN) to highlight the fine-structure and spatial characteristics of the retinal images.

- The Double Angle Formula for Cosine-Contrast Limited Adaptive Histogram Equalization (DAFC-CLAHE) is used in the proposed study to improve the FIs' resolution and highlight the delicate and thin retinal patterns.

- For improving the resilience of the model, the research methodology is generalized well enough for categorizing the multi-grades of the DR, including no DR, mild NPDR, moderate NPDR, severe NPDR, and PDR.

The paper is structured as: The related surveys are exhibited in Section 2; the mathematical modelling of the proposed work is derived in Section 3; the proposed work's performance is validated in Section 4; the paper is concluded with future enhancements in Section 5.

2. RELATED SURVEY

The role of DL and various segmentation algorithms in DR detection and stage classification regarding RFIs is examined as follows,

(Qureshi et al., 2021) incorporated active DL-centric DR detection and stage classification using eye FIs. To classify several DR stages, the active DL-CNN was utilized. The chance of vision impairment was significantly reduced by this approach. Nevertheless, due to the complex retinal patterns, this model had a high misclassification rate. Furthermore, (Das et al., 2021) implemented DL-centric DR classification centered on fundus image segmentation. Here, the FIs were pre-processed, followed by segmentation. Further, for extracting the branching blood vessels, the maximal principal curvature was applied. In the meantime, to refine the segmented regions, morphological opening was utilized. Lastly, to classify the DR, the CNN was employed. This framework helped to improve the personalized treatment plans. Yet, owing to the elimination of false region segmentation, this approach had the maximum risk of contextual information loss. (Kalyani et al., 2023) used a capsule network to develop an effective DR detection and classification framework. Here, an input RFI was fed into the capsule network, which automatically extracted the features from the retinal images. Thereafter, the capsule network categorized the DR stages, such as stage 0, 1, 2, and 3. This model had better diagnosis outcomes, which reduced the risk of blindness. Nevertheless, this approach was sensitive to the choice of initial hyperparameters, which increased the complexity of the model.

During DR classification, the existing works incorporated TL to ensure the generalizability of the model. The TL's contributions in conventional frameworks are given as follows,

(Dutta et al., 2021) presented a robust DR grading system centered on retinal lesion extraction using digital FIs. To classify the multi-grades (no DR, mild NPDR, moderate NPDR, severe NPDR, and PDR) of the DR, a fine-tuned variant of VGG-19 with a TL approach was implemented. This approach had higher adaptability and robustness in DR staging. Nevertheless, owing to the low-resolution FIs, this framework had poor classification outcomes. Furthermore, (Hu et al., 2022) introduced a graph adversarial TL-based DR classification. Here, to perform efficient DR detection, an improved graph neural network was utilized. This approach effectively addressed the intra- and inter-domain alignment issues due to the inclusion of TL. However, this model struggled to capture the crucial information associated with the subtle and overlapping retinal lesions, thereby exhibiting poor generalizability.

The conventional studies that incorporate multi-level feature learning in DR classification are surveyed as follows,

(Xu et al., 2024) recommended a computer-assisted diagnosis of DR using multi-view joint learning. Here, to classify the DR into several stages, a robust two-branch network that integrated EfficientNet (EN) and multi-feature fusion was employed. Owing to the inclusion of local and global feature patterns, this framework had better learning capability. However, as a result of the structural resemblance between vessels and surrounding retinal tissues, this existing work struggled to isolate the retinal blood vessels. In addition, (Usman et al., 2023) presented a multi-level feature extraction-based DR detection using Principal Component Analysis (PCA). Centered on the pre-trained CNN, a multi-label feature classification was done. Therefore, through early DR detection, proactive treatment was provided by the suggested approach, reducing the disease progression. Yet, this framework didn't handle patients with different vessel patterns as well as lesion appearances.

To improve the efficacy of the DR grading, the majority of the traditional studies utilized bio-inspired meta-heuristic optimization methods, such as butterfly optimization and tunicate swarm optimization. Hence, the optimization-integrated DR classification studies are explored further,

(Dayana & Emmanuel, 2022) established an improved swarm optimization-assisted DNN for DR diagnosis based on FIs. Initially, the low-quality FIs were pre-processed and further fed into the segmentation phase. Afterward, to perform DR classification, the feature extraction was carried out. Eventually, the bio-inspired tunicate swarm optimization-based deep stacked autoencoder was established. This approach had minimal computation time and maximal accuracy. However, this framework didn't considerably capture the fine structural and spatial patterns of the retinal images, leading to limited efficiency. Similarly, (Özbay, 2023) developed an effective DR detection centered on segmented FIs utilizing DL and an artificial bee colony algorithm. In the FIs, the threshold-centric segmentation was done. Subsequently, to categorize DR, the tag-efficient CNN was employed. The segmented vessels and lesions were efficiently handled by this approach, optimizing its performance. Nevertheless, owing to the inappropriate thresholding scheme, this framework had over-segmentation and under-segmentation issues. (Rachapudi et al., 2023) executed a DR detection based on butterfly optimization to provide an optimized DL approach. Primarily, the RFIs were pre-processed, followed by GC extraction and contrast enhancement. After that, to categorize several stages of the DR, features were extracted and inputted to the DNN with the butterfly optimization algorithm. In DR staging, this framework had better dominance. Nevertheless, due to the high-dimensional features, this approach had substantial computational overhead issues.

Table 1 depicts the conventional studies' in-depth comparative analysis.

Table 1: Comprehensive Survey Of The Existing DR Classification Frameworks

Authors' name	Target area	Dataset	Algorithm	Findings	Limitations
(Qureshi et al., 2021)	An active DL-centric DR detection and stage classification using eye FIs	EyePacs dataset	Active DL-CNN	Accuracy – 98% Specificity – 95.10 %	However, due to the complex retinal patterns, this model had a high misclassification rate.
(Das et al., 2021)	DL-based DR classification centered on fundus image segmentation	DIARETDB1 (standard DR Dataset)	CNN	Accuracy - 98.7 % Precision - 97.2 %	Nevertheless, owing to the elimination of false region segmentation, this approach had the maximum risk of contextual information loss.
(Xu et al., 2024)	A computer-assiste	EyePACS and APTO	EN and multi-feature	Accuracy – 85.4	However, owing to the structura

	d diagnosis of DR using multi-view joint learning	S 2019	fusion	% Precision – 82.4 %	l resemblance between vessels and surrounding retinal tissues, this existing work struggled to isolate the retinal blood vessels.
(Dutta et al., 2021)	A robust DR grading system centered on retinal lesion extraction using digital FIs	DR detection dataset	A fine-tuned variant of VGG-19 with a TL approach	Accuracy – 77% Specificity – 78.5 %	However, owing to the low-resolution FIs, this framework had poor classification outcomes.
(Usman et al., 2023)	A multi-level feature extraction-based DR detection using PCA	DR detection dataset	Pre-trained CNN	Accuracy - 93.67 %	Nevertheless, this framework didn't handle patients with diverse vessel patterns and lesion appearances.
(Dayana & Emmanuel, 2022)	An improved swarm optimization-assisted DNN for DR diagnosis based on FIs	DIAR ETDB 0 and DIAR ETDB 1	Bio-inspired tunicate swarm optimization-centric deep stacked autoencoder	Accuracy – 78.6 % Sensitivity – 71.7 %	But, this framework failed to considerably capture the fine structural and spatial patterns of the retinal images, leading to limited efficiency.
(Özbay, 2023)	An effective DR detection centered on segmented FIs using DL and an artificial bee colony algorithm	EyePacs dataset	Tag-efficient CNN	Sensitivity - 93.76 % Specificity - 96.71 %	Yet, owing to the inappropriate thresholding scheme, this framework had over-segmentation and under-segmentation issues.
(Hu et al., 2022)	A graph adversarial TL-based DR classification	EyePACS dataset	An improved graph neural network	Accuracy - 92.7 %	However, this model struggled to capture the crucial information associated with the subtle and overlapping retinal

					lesions, exhibiting poor generalizability.
(Kalyani et al., 2023)	An effective framework called DR detection and classification based on a capsule network	Messidor dataset	Capsule network	Accuracy - 97.98 %	However, this approach was sensitive to the choice of initial hyperparameters, augmenting the model's complexity.
(Rachapudi et al., 2023)	A DR detection using an optimized DL approach	DIARETDB1 and Messidor dataset	DNN with the butterfly optimization algorithm	Accuracy - 98.3 %	However, due to the high-dimensional features, this approach had significant computational overhead issues.

In the above-mentioned studies, various algorithms, such as CNN, capsule network, VGG-19, and EN, were utilized for the classification of the multiple grades of DR. The existing approaches helped to enhance the treatment strategies and prevent blindness in DR patients through early detection. Yet, during DR classification, the traditional algorithms faced several challenges. The conventional strategies had maximum contextual information loss owing to ineffective region segmentation and had a misclassification rate due to complex retinal patterns. Furthermore, the traditional approaches were sensitive to the choice of initial hyperparameters, thereby displaying higher complexity. The existing work had limited classifier performance owing to the poor resolution of FIs. Due to the structural similarity between vessels and surrounding retinal tissues, some conventional techniques struggled to segment the retinal blood structure. The absence of TL limited the model's capability of handling patients with various vessel patterns and lesion appearances. Thus, the proposed work is motivated by the requirement to diminish the above-mentioned problems of the conventional studies. Here, the proposed DAFC-CLAHE is generalized well enough for improving the FIs' resolution, facilitating better detection of subtle lesions. The proposed TCLLKEN performs an adaptive and effective weight parameter initialization to reduce the model's complexity. Additionally, the TL is incorporated with the proposed classifier to adapt to patients with diverse retinal structures. The proposed work introduces the GC extraction to effectively isolate the blood vessels. Effective region grouping is carried out in the proposed work to capture the fine structural and spatial features of the retinal patterns, decreasing the misclassification rate.

3. PROPOSED METHODOLOGY FOR VLS-AWARE MULTI-GRADE DR CLASSIFICATION USING TCLLKEN

The proposed work implements an enhanced multi-grade DR classification approach with VLS analysis centered on the RFIs using TCLLKEN. In addition, VLS, including loop degree, loop count, and loop area from the vessel graphs, is accurately extracted in the proposed work, thus augmenting the significance of the DR grading. Figure 1 depicts the proposed work's pictorial depiction.

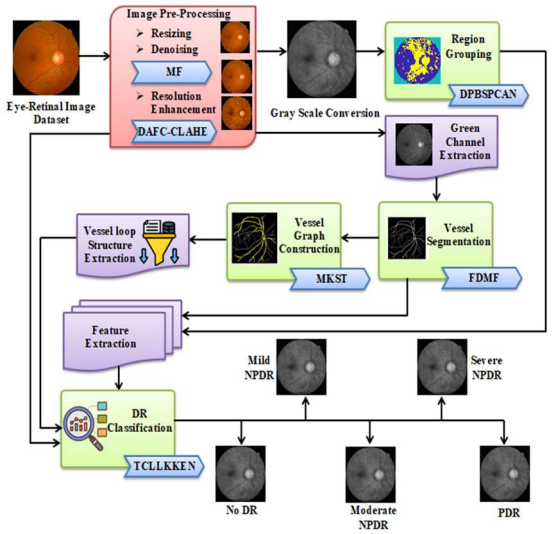

Figure 1: Structural Design Of The Research Methodology

In the proposed approach, the fundamental targets, namely pre-processing, region grouping, GC extraction, vessel segmentation, vessel graph construction, VLS extraction, and multi-grade DR classification, are mainly encompassed. Thus, the comprehensive overview of the proposed DR classification is given as follows,

3.1 Eye retinal image collection

Initially, to train the proposed DR classification framework, eye RFIs are gathered from publicly available sources. By utilizing the fundus camera that captures the retina's inner structure, Eye RFIs are acquired. The collected eye retinal images' initialization is articulated in equation (1) as,

$$\hat{a}_y = \left(\hat{a}_1, \hat{a}_2, \ldots\ldots \hat{a}_Y\right) \text{ Here, } y = 1 to Y \tag{1}$$

Where, the number of collected eye retinal images $\hat{a}_y$ is depicted as Y. After that, $\hat{a}_y$ are subjected to the image pre-processing.

3.2 Image pre-processing

In general, noises and poor resolution are involved in the raw $\hat{a}_y$, affecting the model's prominence and DR prediction outcomes. Thus, the pre-processing steps like resizing, denoising, and resolution enhancement are performed in the proposed work.

- **Resizing**

The process of standardizing the image dimensions of each φ_y into the same dimensions is referred to as resizing, which reduces the computational cost. The mathematical representation of the process of resizing is depicted in equation (2) as,

$$\hat{a}_y \xrightarrow{\text{resize}} \Re \tag{2}$$

Here, the resized images are signified as $\Re$.

- **Denoising**

Thereafter, the resized images $\Re$ are subjected to denoising, in which the irrelevant noises caused by camera sensors and patient movement are removed while preserving the images' edge properties. To perform denoising, the proposed work employs the Median Filter (MF), which enhances the visibility of retinal structures. A non-linear technique utilized for eliminating noise through replacing the value of each pixel with the median value of the intensities in its neighbourhood window is termed MF. The computation of the MF is exhibited in equation (3) as,

$$\overline{N}\left(\ddot{a}, \ddot{b}\right) = \underset{(a,b)\in\rho_{\ddot{a}\ddot{b}}}{\text{median}}\left\{\Re(a,b)\right\} \tag{3}$$

Where, the denoised images with pixel coordinates $\left(\ddot{a}, \ddot{b}\right)$ are specified as $\overline{N}\left(\ddot{a}, \ddot{b}\right)$, the median operation is indicated as median , the window function is exemplified as ρ, and the pixel coordinates of the resized images are given as (a,b).

- **Resolution enhancement**

Here, using the proposed DAFC-CLAHE, the low resolution of the denoised images $\overline{N}$ is enhanced into high resolution. Traditional Contrast Limited Adaptive Histogram Equalization (CLAHE) has a high adaptive nature, thus permitting it to dynamically adjust contrast based on the local properties of each frame. However, owing to the

inappropriate contrast-limited step, the traditional CLAHE has a risk of over-enhancement or under-enhancement. The prevailing CLAHE depends heavily on heuristic clip limits or dataset-dependent clip limits. The proposed work employs the Double Angle Formula for Cosine (DAFC) to set the proper clip limit. The DAFC calculates the clip limit by considering the image intensity distribution to an optimal scaling factor that controls resolution improvement. Therefore, adaptive and resolution-preserving contrast enhancement is ensured by the inclusion of DAFC. Hence, the efficiency of the contrast enhancement is increased by an enhanced DAFC-CLAHE.

Primarily, to enable local region enhancement, the input image η is segmented into numerous non-overlapping blocks (tiles), which is depicted in equation (4) as,

$$\bar{N} \xrightarrow{\text{divide}} \left\| \tilde{t}_1, \tilde{t}_g, \ldots . \tilde{t}_G \right\| \tag{4}$$

Where, the number of segmented tiles $\left(\tilde{t}_g\right)$ is denoted as $g = 1 to G$. The histogram of pixel intensities (λ) is calculated for each tile to showcase the local distribution of gray levels. The histogram is estimated by utilizing equation (5) as,

$$\lambda \rightarrow \sum_{q=1}^{Q} \tilde{t}_g ; q \in (0, Q-1) \tag{5}$$

Here, the number of gray levels in the τ_g is indicated as $q = 1,2,\ldots Q$. By using the DAFC, a clip limit $\left(\vec{L}\right)$ is applied to mitigate over-enhancement. If the limit is exceeded by any histogram bin, then the excess counts are redistributed equally across all bins. The clip limit selection and clipped histogram are notated in equations (6) and (7), respectively.

$$\vec{L} = \tilde{t}_g \left(\cos^2 \theta - \sin^2 \theta\right) \tag{6}$$

$$\lambda^{\text{clip}} = \min\left(\lambda(q), \vec{L}\right) \tag{7}$$

Where, the cosine function is displayed as $\cos$, the coefficient of theta is illustrated as θ, the sine function is depicted as $\sin$, and the clipped histogram is represented as λ^{clip}. The Cumulative Distribution Function (CDF) $\left(Z(q)\right)$ is computed for the clipped histogram in each tile to redistribute the pixel intensity values within a localized region of an image. The formula for CDF is depicted in equation (8) as,

$$Z(q) = \sum_{q=0}^{Q} \frac{\lambda^{\text{clip}}(q)}{O} \tag{8}$$

Here, the total number of pixels in the tile τ_g is signified as O. Based on the $Z(q)$, each pixel intensity in the tile is transformed. By using equation (9), new pixels that need to be replaced in the poor resolution images are computed as,

$$\partial^{\text{new}} = \hat{\lambda}_{\min} + \left(\nu_{\max} - \hat{\lambda}_{\min}\right) \cdot Z(q) \tag{9}$$

Where, the new pixels are depicted as ∂^{new}, the minimum intensity range is given as $\hat{\lambda}_{\min}$, and the maximum intensity range is specified as $\nu_{\max}$. Eventually, the bilinear interpolation is applied for the prevention of blocky artifacts at tile boundaries. The bilinear interpolation confirms that the pixel values are smoothly blended among neighbouring tiles. Therefore, the resolution-enhanced (pre-processed) images are shown as $\left(\hat{\text{N}}\right)$.

3.3 Gray scale conversion

The gray-scale conversion is done in $\hat{\text{N}}$ to improve the visibility of small lesions. The task of converting the color fundus image to a single intensity channel is called gray-scale conversion. Red, Green, and Blue (RGB) retinal images are simplified into single-channel intensity maps by grayscale conversion, enhancing the lesion visibility and performance of DR detection. The conversion process of the RGB to the gray scale is depicted in equation (10) as,

$$\hat{G} = 0.2989 \cdot r + 0.5870 \cdot \hbar + 0.1140 \cdot \iota \tag{10}$$

Where, the grayscale converted images are depicted as $\hat{G}$, the red channel is demonstrated as r, the GC is illustrated as $\hbar$, and the blue channel is notated as $\imath$. Grayscale conversion enhances the patterns' visibility without the interference of color information.

3.4 Region grouping

Using the proposed DPBSPCAN, the retinal regions like lesions are grouped from $\hat{G}$ based on their similar pixel intensities, thereby capturing fine-structure and spatial features of the retinal patterns. Lesions of arbitrary shapes are automatically detected by the conventional Density-Based Spatial Clustering of Applications with Noise (DBSCAN). Additionally, the DBSCAN has high adaptability and robustness. Nevertheless, due to the effective clustering parameter initialization technique, the existing DBSCAN is sensitive to the choice of clustering parameters like epsilon and min-pts. Suboptimal clustering results are caused by improper parameter selection. Thus, to determine the epsilon parameter, the Prony Equation (PE) is employed in the proposed work. By approximating pixel information with a sum of exponentials, the PE estimates the suitable epsilon. The research methodology establishes the Probability Density Function (PDF) to select the proper minpts. The PDF dynamically selects MinPts regarding actual data density, making clustering outcomes more accurate. The clustering parameters like minpts and epsilon are adaptively selected through the inclusion of PE and PDF, thereby grouping the regions effectively than existing DBSCAN. Hence, the enhanced DBSCAN is known as DPBSPCAN, which is further described.

- At first, to initiate the cluster process, the parameters like epsilon and the minimum number of points (MinPts) are defined. Epsilon is referred to as the maximum distance between two points, signifying the radius of the neighborhood. Here, using PE, the epsilon (ς) is selected, which is shown in equation (11) as,

$$\varsigma = \frac{U}{\mu}\left(\sigma \mathrm{I} + \Theta \mathrm{I}^2\right) \tag{11}$$

Here, the number of pixel intensities is indicated as U, the data dimensionality is depicted as μ, the linear density coefficient is represented as σ, the quadratic density coefficient is exhibited as Θ, and the neighbourhood distance is specified as I.

- Similarly, the minimum number of points needed within the epsilon's neighborhood is termed MinPts (υ). In the proposed work, the PDF is used to choose the suitable MinPts by evaluating how densely data points are distributed across regions. The MinPts selection using PDF to identify the neighbour points is depicted in equation (12) as,

$$\upsilon = \frac{1}{\psi\sqrt{2\pi}} \exp\left(-\frac{1}{2}\left(\frac{\hat{G}-\omega}{\psi}\right)^2\right) \tag{12}$$

Here, the variance and mean of the $\hat{G}$ are shown as ψ and ω, respectively, the exponential term is signified as $\exp$, and the mathematical constant is specified as π.

- Afterward, based on the computed epsilon and MinPts, the points (f) are categorized into core points (Cr), border points (Br), and noise (Ns). A point that has enough neighbours $\ddot{\mathrm{N}}(f)$ around it within the epsilon radius is called a core point. Border point is the point that doesn't have enough neighbours by itself; however, it is close $(\in)$ enough to a core point. Likewise, the point that is too far away $(\notin)$ from the others is referred to as a noise point. In equation (13), the point categorization is expressed as,

$$\begin{cases} \mathrm{If}\left(\ddot{\mathrm{N}}(f) \geq \upsilon\right), & \mathrm{Cr} \\ \mathrm{If}\left(\ddot{\mathrm{N}}(f) < \upsilon\right) \& \; f \in \mathrm{Cr}, & \mathrm{Br} \\ \mathrm{If}\left(\ddot{\mathrm{N}}(f) < \upsilon\right) \& \; f \notin \mathrm{Cr}, & \mathrm{Ns} \end{cases} \tag{13}$$

- Centered on the core point, a new cluster is formed through the addition of the closest data points. The epsilon neighbourhood is analyzed for each point added to the cluster. If a neighbour is also a core point or border point, then the neighbour is added to the same cluster.

On the contrary, the noise points are isolated from the clustering space. In equation (14), the clustering process is mathematically represented as,

$$\begin{cases} \text{If}\left(\ddot{\text{N}}(f) = \text{Cr} \mid \text{Br}\right), & \text{add} \\ \text{If}\left(\ddot{\text{N}}(f) = \text{NS}\right), & \text{isolate} \end{cases} \tag{14}$$

- The clustering process is repeated iteratively till all the data points are marked as visited. Here, the region-grouped data is exhibited as (κ).

3.5 Green channel extraction

Conversely, from $\hat{\text{N}}$, the GC is extracted for enhancing the vessel and lesion contrast, thereby effectively outlining the thin vessel structure. The task of separating the green components from a color image to create a single-channel image that emphasizes features like blood vessels in FIs is known as GC extraction. Primarily, the color image $\hat{\text{N}}$ is segmented into its individual color components. Every single color component signifies the intensity of RGB at each pixel in the original image. Next, since GC renders the highest contrast among features like blood vessels and the surrounding background, it is selected. The GC optimizes the visibility of retinal blood vessels than other channels. Therefore, the extracted GC (Ξ) is fed to the vessel segmentation.

3.6 Vessel segmentation

Here, from Ξ, the vessel structure is segmented centered on the proposed Frangi De Moivre's Filter (FDMF). The traditional Frangi Filter (FF) substantially emphasizes line-like and curvilinear structures, including vessels, while suppressing blob-like regions. Moreover, by applying filters at multiple scales, the existing FF effectively captures vessels of different diameters. However, the traditional FF struggles to choose the substantial scale range, leading to over-segmentation or under-segmentation issues. Therefore, De Moivre's Formula (DMF) is introduced in the proposed work to select the optimal scale range, increasing the segmentation efficiency. The proposed FDMF refers to a multiscale vessel enhancement technique utilized for detecting vessel-like structures by examining the local image structure at multiple scales using the Hessian matrix and its eigenvalues. When contrasted with the conventional algorithm, the proposed work proficiently segments the vessel-like structure by incorporating the DMF-based optimal scale range selection.

Firstly, the image is convoluted with Gaussian kernels $(\hat{\lambda}_{\text{filter}})$ at diverse scales (de), thus allowing the filter to detect vessels of varying widths. By applying the kernels, Equation (15) filters the image, thereby effectively capturing the vessel patterns.

$$\hat{\Theta}(q,p) = \hat{\lambda}_{\text{filter}}{}^{\text{de}} * \Xi \tag{15}$$

Where, the Gaussian-filtered image with pixel coordinates (q,p) is represented as $\hat{\Theta}(q,p)$.

The Hessian matrix $(\tilde{\text{H}})$ is computed for each pixel in $\hat{\Theta}(q,p)$ to represent the second-order partial derivatives (local image structure) of the $\hat{\Theta}(q,p)$. Curvature information is captured by the Hessian matrix. The proposed work uses the DMF in the Hessian matrix calculation to determine the scale range, which is presented in equation (17). The Hessian matrix is calculated by utilizing equation (16) as,

$$\tilde{\text{H}}(q,p,\nu) = \left(\zeta_{qq}(q,p,\nu)\zeta_{qp}(q,p,\nu)\zeta_{pq}(q,p,\nu)\zeta_{qq}(q,p,\nu)\right) \tag{16}$$

$$\nu = \cos\left(\iota\hat{\Theta}\right) + \text{Ig}\cdot\sin\left(\iota\hat{\Theta}\right) \tag{17}$$

Here, the scale range is indicated as ν, the second-order partial derivatives are represented as ζ_{pq}, ζ_{qp}, and ζ_{qq}, the integer exponent is specified as ι, and the imaginary unit is represented as Ig. Furthermore, the Hessian matrix's eigenvalues $(\wp_1, \wp_2)$ are computed to define whether the local structure looks like a line/vessel or blob. To determine the vesselness, the eigenvalues are computed, and it is given in equation (18).

$$\wp_1, \wp_2\left(\tilde{\mathrm{H}}\right) = \frac{\mathrm{xy}+\mathrm{Cy}}{2} \pm \sqrt{\left(\frac{\mathrm{xy}-\mathrm{Cy}}{2}\right)^2 + \mathrm{bc}} \tag{18}$$

Where, the modulus of $\tilde{\mathrm{H}}$ is depicted as xy, the control parameter is indicated as Cy, and the cross-derivative term of the hessian matrix is specified as bc. The blobness ratio $\left(B^{\mathrm{ratio}}\right)$ and structureness $\left(S^{\mathrm{ness}}\right)$ are computed based on the eigenvalues to measure the geometric nature, which is shown in equations (18) and (19).

$$B^{\mathrm{ratio}} = \frac{|\wp_1|}{|\wp_2|}; \quad \mathrm{if}\left(\wp_2 \neq 0\right) \tag{19}$$

$$S^{\mathrm{ness}} = \sqrt{\wp_1{}^2 + \wp_2{}^2} \tag{20}$$

Further, to assign a vesselness score $\left(V^{\mathrm{score}}\right)$ to each pixel, Frangi's formula is computed. The pixel with a high score specifies the vessel-like structure, whereas the pixel with a low score represents the background or noise. The vesselness score computation is articulated in equation (21).

$$V^{\mathrm{score}}\left(\hat{\Theta}\right) = \begin{cases} 0, & \mathrm{if}\left(\wp_2 > 0\right) \\ \exp\left(-\frac{B^{\mathrm{ratio}}_T}{2T^2}\right)\left(1-\exp\left(-\frac{S^{\mathrm{ness}^2}}{2\mathrm{Cy}^2}\right)\right), & \mathrm{else} \end{cases} \tag{21}$$

Where, the control parameter of the blobness ratio is denoted as T, and the exponential function is notated as $\exp$. The high vesselness score over all scales (different diameters) is considered for each pixel to generate the binary mask, ensuring that the vessels of different widths are captured. From the RFIs, the vessel structures are isolated based on the vessel binary mask, which is represented in equation (22).

$$\Omega \xleftarrow{\text{isolate}} \Xi \tag{22}$$

Next, the segmented vessel Ω is inputted into the vessel graph construction.

3.7 Vessel graph construction

Thereafter, using the proposed MKST, the vessel graph structure is constructed from the segmented blood vessels Ω. The traditional Minimum Spanning Tree (MST) has high computational efficiency and better graph representation. The prevailing MST maintains the skeleton-like backbone of the vessel tree while pruning unnecessary branches, aligning well with the real vascular tree. Nevertheless, due to the random edge weight selection, the existing MST has unstable graph construction outcomes. Random weight selection is not always appropriate. Therefore, to select the edge weight, Kepler's Equation (KE) is introduced in the proposed work, enhancing the connectivity efficiency. KE ensures non-random edge weight selection, evading instability in graph construction and vessel structure analysis. Thus, by effectively selecting the suitable weights using the KE, an improved MKST performs better than the existing MST.

At first, the edges (vessel pixels) and vertices (connectivity points) are identified. Thereafter, to initiate the graph construction, a random vertex $\left(\mathrm{o}\right)$ is included in the graph matrix. The graph matrix initialization is depicted in equation (23).

$$\mathrm{o}\left(\Omega\right) \xrightarrow{\text{visit}} G_{\mathrm{matrix}} \tag{23}$$

Where, the graph matrix is given as G_{matrix}. Subsequently, in equation (24), the set of visited vertices (start vertex) and a set of unvisited vertices (other vertices) are initialized.

$$\left(\mathrm{Vi}, \mathrm{UN}\right) = \sum_{i,k=1}^{I,K} \left(Vi_i, UN_k\right) \tag{24}$$

Here, the number of visited Vi and unvisited vertices UN is denoted as $i = 1 to I$ and $k = 1 to K$, respectively. Moreover, for each edge, the weight value $\left(\mathrm{Wu}\right)$ is assigned using the KE, which is exhibited in equation (25).

$$\mathrm{Wu}(\mathrm{Ed}) = \ddot{\mathrm{O}} - \mathrm{i}'''\sin\ddot{\mathrm{O}} \tag{25}$$

Where, the eccentric anomaly of the edges Ed is notated as $\dddot{\mathrm{O}}$, and the eccentricity of the edges Ed is represented as i'''. Thereafter, the edge with the minimum weight is considered for connecting the visited edge with the unvisited edge. In equation (26), the edge connection is mentioned.

$$\mathrm{Ed} \xrightarrow{\text{connect}} \min(\mathrm{Wu}) \tag{26}$$

The graph construction process is repeated iteratively till all vertices are visited. Hence, the constructed vessel graph is depicted as $(\hat{\mathrm{A}})$. The proposed MKST's pseudocode is displayed as follows,

Input: Segmented blood vessels Ω

Output: Constructed vessel graph $\hat{\mathrm{A}}$

Begin

Initialize Ω, o, G_{matrix} and Wu

For 1 to each Ω do,

Determine edges and vertices

Initiate graph connection

$$\mathrm{o}(\Omega) \xrightarrow{\text{visit}} G_{\text{matrix}}$$

List visited and unvisited vertices

$$(\mathrm{Vi}, \mathrm{UN}) = \sum_{i,k=1}^{I,K} (Vi_i, UN_k)$$

Assign edge weights

$$\mathrm{Wu}(\mathrm{Ed}) = \ddot{\mathrm{O}} - \mathrm{i}'''\sin\ddot{\mathrm{O}}$$

Connect

$$\mathrm{Ed} \xrightarrow{\text{connect}} \min(\mathrm{Wu})$$

End For

Return $\hat{\mathrm{A}}$

End

Further, the VLS extraction is carried out.

3.8 Vessel loop structure extraction

The important VLSs like loop degree, loop area, and number of loop counts are extracted from the constructed vessel graph $\hat{\mathrm{A}}$ to improve the efficiency of the early DR outcomes. Quantitative biomarkers of vascular abnormalities are offered by loop features. The essential biomarker for recognizing the DR is the vessel loop. Owing to the transition from early-stage DR (NPDR) to PDR, vessel loops are created. Therefore, to improve the reliability of the DR prediction outcomes, timely DR classification is essential. Excessive neovascularization is emphasized by the loop count $\left(L^{\text{count}}\right)$. The abnormal vessel connectivity and branching are indicated by the loop degree $\left(L^{\deg}\right)$, and pathological vessel dilation is identified by the loop area $\left(L^{\text{area}}\right)$. In equations (27), (28), and (29), the mathematical formulas for loop area, loop count, and loop degree are shown, respectively.

$$L^{\text{area}} = 0.5\left|(\mathrm{uv}, \mathrm{xy}+1) - (\mathrm{uv}+1, \mathrm{xy})\right| \tag{27}$$

$$L^{\text{count}} = |\mathrm{Ed}| - |\mathrm{Vi}| + \ddot{\sigma} \tag{28}$$

$$L^{\deg} = \frac{1}{|\mathrm{LO}|}\sum \deg(\mathrm{Vi}) \tag{29}$$

The total number of extracted VLS is indicated in equation (30).

$$\mathrm{Lp}_y = (\mathrm{Lp}_1, \mathrm{Lp}_2, \ldots\ldots \mathrm{Lp}_Y) \text{ Here, } y = 1 to Y \tag{30}$$

Where, the number of extracted vessel loop features Lp_y is illustrated as Y, the set of vertices belonging to loops is notated as LO, the degree function is exhibited as $\deg$, the number of connected edges is specified as $\ddot{\sigma}$, and the coordinates of loop boundary vertices are represented as $(\mathrm{uv}, \mathrm{xy})$.

3.9 Feature extraction

Here, the segmented vessels and region-grouped images are fed into the feature extraction phase. The process of extracting the significant properties of the images for optimizing the learning capability of the proposed DR classification module is known as feature extraction. From the pre-processed image,

the essential features like average intensity, mean intensity, standard deviation of intensity, maximum pixel values, contrast, minimum pixel values, entropy, intensity variance, homogeneity, energy, local binary pattern, spatial features, branching patterns, bifurcation points, vessel thickness variation, uniformity of vessel structure, and vessel density are extracted. The features like shape, area, compactness, eccentricity, roundness, and diameter are extracted from the region-grouped images, as shown in equation (31).

$$\Re_e''' = \left\langle \Re_1''', \Re_2''', \ldots\ldots \Re_E''' \right\rangle \text{ Where, } e = 1,2,\ldots E \quad (31)$$

Here, the number of extracted features $\Re_e'''$ is given as E .

3.10 DR classification

Lastly, Lp_y , extracted features($\Re_e'''$), and pre-processed images($\hat{\mathrm{N}}$) are fed to the proposed TCLLKEN that carries out multi-grade DR classification. In the traditional EN, a compound scaling method that balances network depth, width, and input resolution is used, permitting the models to achieve better accuracy. Moreover, the conventional EN has better feature extraction and higher robustness to image variations. Nevertheless, owing to improper neuron activation, the existing EN has reduced non-linearity and vanishing gradient issues. As a result of the traditional activation functions like sigmoid or the Rectified Linear Unit, the existing EN is less effective. Hence, to introduce the non-linearity and improve the neuron's learning efficiency, the proposed work employs the Complementary Log-Log (CLL) activation. Yet, due to the random weight parameter initialization, the existing EN has gradient instability issues. The risk of dead neurons is increased by an improper weight initialization. Therefore, to regularize the suitable weight values, the proposed work utilizes the Karplus Equation (KPE), showing model stability. KPE chooses a weight value that balances the interaction between neurons, evading extremely large or small values. In the proposed approach, TL is introduced to adapt to the various patients' information. Overall, when compared with the traditional EN, an improved TCLLKEN is better due to the novel inclusion of effective weight regularization, proper neuron activation, and TL integration. Figure 2 indicates the proposed TCLLKEN's structure.

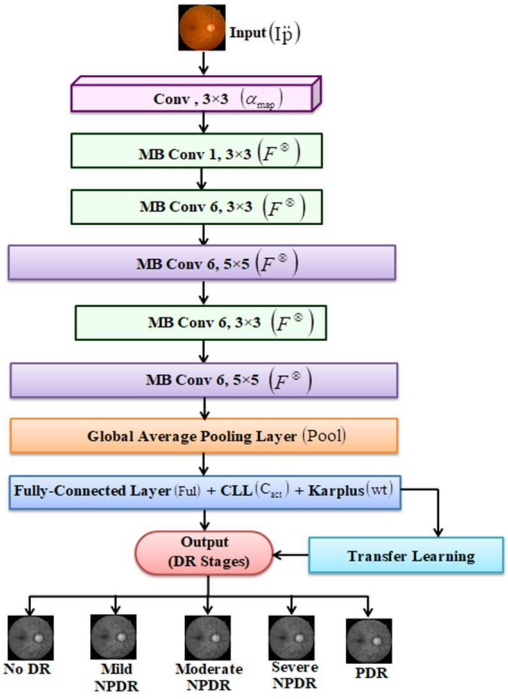

Figure 2: The Architecture Of The Proposed TCLLKEN

Primarily, a compound scaling (ϕ''') scheme is utilized for improving the network's depth $(\varsigma_{\oplus})$, width $(\aleph^{\infty})$, and resolution $(\overline{\varpi})$ regarding the compound coefficient (Ψ). The compound scaling permits the model to capture finer details in input images while optimizing overall accuracy. Equation (32) illustrates the compound scaling.

$$\phi''' = \left\langle \varsigma_{\oplus}, \aleph^{\infty}, \overline{\varpi} \right\rangle \quad (32)$$

Here, the inputs $(\mathrm{Iṗ})$ like Lp_y , $\Re_e'''$, and $\hat{\mathrm{N}}$ are inputted into the convolutional layer, which generates the feature map (α_{map}) automatically. In equation (33), the kernel and padding are applied with a stride to create the feature map.

$$\alpha_{\mathrm{map}} = \left(\left(\mathrm{Iṗ} - \mathrm{K}_{\mathrm{size}} + 2 \times \mathrm{Pd} \right) / \mathrm{sd} \right) + 1 \quad (33)$$

Where, the kernel size is indicated as K_{size}, the padding of the Ip̈ is signified as Pd, and the stride of the Ip̈ is notated as sd. Thereafter, the feature map is processed through a set of Mobile inverted Bottleneck convolutional layers (MBConv) with different configurations. To obtain crucial spatial details, MBConv utilizes depth-wise separable convolution (D_{wise}) and 1x1 point-wise convolution (Φ). Here, the 1x1 convolution is applied for increasing the number of channels, acquiring the most relevant features $(F^{\otimes})$. By utilizing equation (34), crucial features are obtained via depthwise convolution and point-wise convolution.

$$F^{\otimes} = D_{wise} * \Phi(\alpha_{map}) \tag{34}$$

Afterward, the global average pooling layer is utilized for reducing the convoluted features' spatial dimensions. In equation (35), the dimensionality-reduced features are mentioned.

$$\text{Pool} = \text{Glob}(F^{\otimes}) \tag{35}$$

Here, the global pooling operation is notated as Glob, and the dimensionality-reduced features are demonstrated as Pool.

Next, the fully connected layer (Ful) efficiently acquires the probability value for different types of DR regarding the reduced feature map. By using equation (36), the fully-connected layer is acquired.

$$\text{Ful} = C_{act} * (\text{Pool} \cdot \text{wt}) + \text{bs} \tag{36}$$

Where, the weight value is indicated as wt, and the bias value is denoted as bs. The proposed work uses CLL activation (C_{act}) to improve the neuron's learning efficiency. The CLL activation is formulated in equation (37) as,

$$C_{act}(\text{Pool}) = 1 - \exp(-\exp|-\text{Pool}|) \tag{37}$$

The proposed work uses the KE to regularize the weight values wt, which is shown in equation (38). KE selects an appropriate weight value that balances the neurons' stability by utilizing the cosine transform, thus diminishing the over-fitting issues.

$$\text{wt} = \text{ab}\cos 2\ell^{\circ} + \text{bc}\cos\ell^{\circ} + \text{cd} \tag{38}$$

Where, the Karplus constant values are illustrated as ab, bc, and cd, and the dihedral torsion angles are indicated as ℓ°.

Furthermore, to handle patients with different lesion appearances and vessel patterns, TL is employed in the proposed work. By reusing the knowledge acquired from another task with limited data, TL (Tl) handles rare patterns, optimizing the model's robustness. Equation (39) renders the mathematical modelling of the TL.

$$\text{Tl}(\text{Ful}) = \left| S^{\text{task}}, D_{\text{task}}(\text{Ip̈}) \right| \tag{39}$$

Here, the source data and targeted data are signified as S^{task} and D_{task}, respectively. Lastly, several stages (no DR, mild NPDR, moderate NPDR, severe NPDR, and PDR) of the DR are effectively classified by the proposed TCLLKEN.

The proposed TCLLKEN's pseudo code is rendered as follows,

Input: Loop structure Lp_y, extracted features $\Re_e'''$ and pre-processed images $\hat{\text{N}}$
Output: Multi-grade DR classification

Begin

Initialize Lp_y, $\Re_e'''$, $\hat{\text{N}}$ and Ip̈

For 1 to each input do,

Perform compound scaling

$$\phi''' = \langle \varsigma_{\oplus}, \aleph^{\infty}, \overline{\varpi} \rangle$$

Apply convolution operation

$$\alpha_{map} = ((\text{Ip̈} - \text{K}_{size} + 2 \times \text{Pd}) / \text{sd}) + 1$$

#MB conv

Evaluate

$$F^{\otimes} = D_{\text{wise}} * \Phi\left(\alpha_{\text{map}}\right)$$

Implement global average pooling

$$\text{Pool} = \text{Glob}\left(F^{\otimes}\right)$$

Execute fully-connected layer,

$$\text{Ful} = C_{\text{act}} * \left(\text{Pool} \cdot \text{wt}\right) + \text{bs}$$

Activate CLL

$$C_{\text{act}}\left(\text{Pool}\right) = 1 - \exp\left(-\exp\left|-\text{Pool}\right|\right)$$

Regularize weight value using KE

Integrate transfer learning

$$\text{Tl}\left(\text{Ful}\right) = \left|S^{\text{task}}, D_{\text{task}}\left(\text{Ip}\ddot{}\right)\right|$$

Classify multi-grade DR

End For

Return DR stages

End

Overall, early DR staging is facilitated by the proposed work, thereby preventing blindness.

4. RESULTS AND DISCUSSION

Here, the proposed work's superiority and robustness are assessed via performance analysis and comparative validation. Furthermore, the proposed work is employed on the PYTHON platform.

4.1 Dataset description

Utilizing the publicly available dataset named Eyepacs, Aptos, and Messidor DR Dataset (EAMDRD), the proposed DR classification framework is assessed. The EAMDRD includes 1,29,442 high-quality RFIs across several stages, encompassing no DR, mild NPDR, moderate NPDR, severe NPDR, and PDR. Additionally, the training and testing sets are involved in the EAMDRD. Table 2 exhibits the dataset samples.

Table 2: *Samples of the EAMDRD*

Class	Training	Testing
No DR	55162	6896
Mild NPDR	18470	1862
Moderate NPDR	24198	2999
Severe NPDR	7936	978
PDR	9475	1466
Total (129442)	115241	14201

The sample image outcomes of the proposed work are given in Table 3.

Table 3: Image Results

Process / Class	No DR	Mild NPDR	Moderate NPDR	Severe NPDR	PDR
Input / Resizing	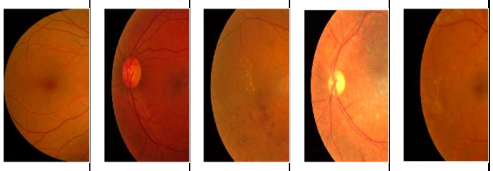				
Denoising	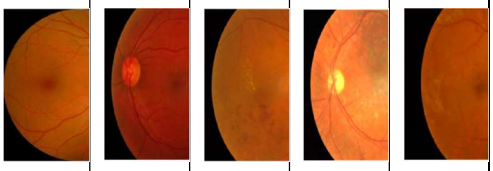				
Resolution enhancement	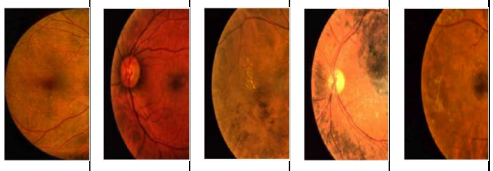				
Gray scale conversion	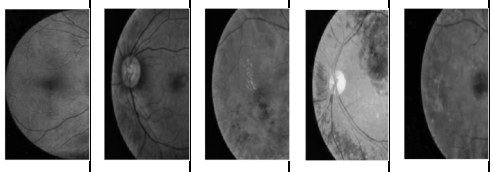				

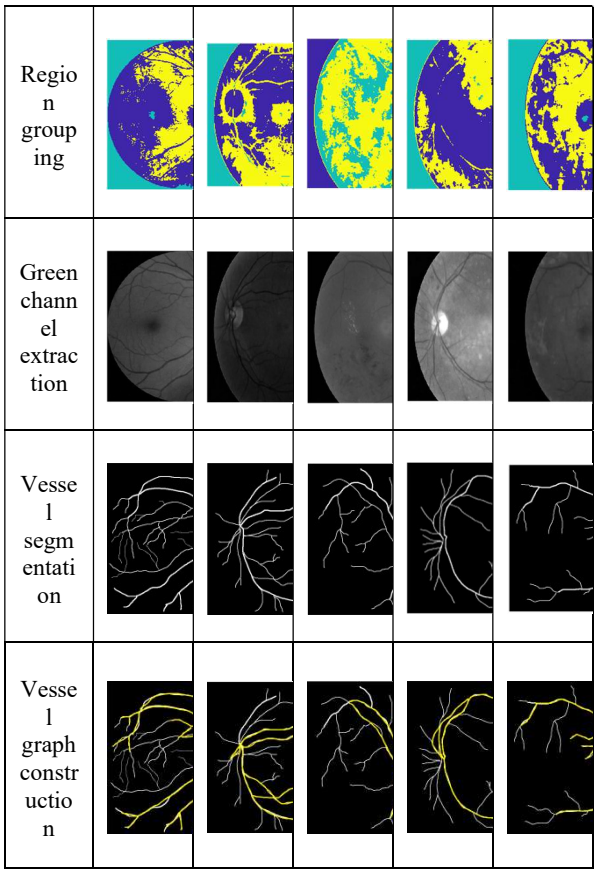

The sample image outcomes of the proposed work regarding input, resizing, denoising, resolution enhancement, gray scale conversion, region grouping, GC extraction, vessel segmentation, and vessel graph construction are presented in Table 3.

4.2 Performance validation of the proposed approach

Regarding several quality metrics like accuracy, precision, Cohen's kappa, Mean Squared Error (MSE), graph construction time, and dice coefficient, the performance analysis is done to prove the superior performance of the model in multi-grade DR classification.

4.2.1 experimental investigation for vessel graph construction

Here, the proposed MKST's performance is validated by contrasting it with several conventional techniques, such as MST, Relative Neighborhood Graph (RNG), Minimum Cycle Basis (MCB), and Steiner Tree Approximation (STA), concerning the vessel graph construction.

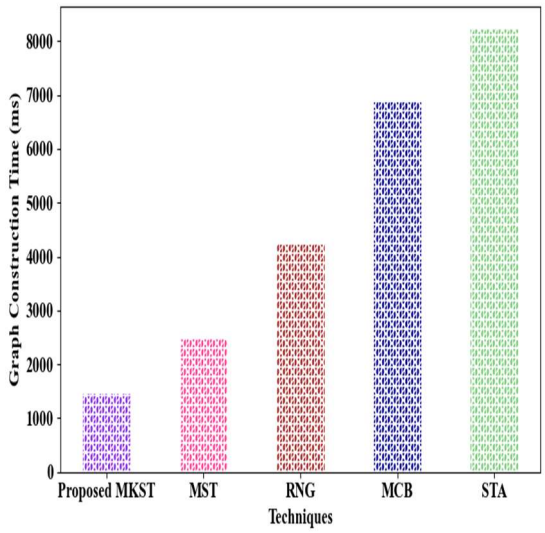

Figure 3: Graph Construction Time Analysis

The graph construction time validation of the proposed MKST and existing graph construction techniques is shown in Figure 3. The graph construction efficiency of the proposed work was enhanced owing to the presence of KE-based edge weight selection. Here, to construct the vessel graph structure, the proposed MKST took 1478ms. Also, a graph construction time of 2482ms was consumed by the conventional MST. Furthermore, an average graph construction time of 5461ms was obtained by the traditional algorithms. Due to the random edge weight selection, the conventional approaches had considerable time complexity. Therefore, as per the analysis outcomes, the proposed work had minimum complexity and maximum efficiency in vessel graph construction.

4.2.2 numerical analysis for multi-grade DR classification

The performance analysis is conducted to showcase the proposed TCLLKEN's robustness in multi-grade DR classification.

Table 4: Experimental Validation For Multi-Grade DR Classification

Methods	Accuracy (%)	Precision (%)	Recall (%)	F-measure (%)	Specificity (%)

Proposed TCLLKEN	98.99	98.99	98.98	98.99	98.97
EN	96.43	96.49	96.58	96.84	96.90
DCNN	94.27	93.59	94.28	94.76	94.29
GRU	92.58	90.88	92.90	92.69	92.58
RNN	89.79	88.75	90.78	90.58	90.57

Table 4 evaluates the proposed TCLLKEN's performance by comparing it with several associated classifiers like EN, Deep CNN (DCNN), Gated Recurrent Unit (GRU), and Recurrent Neural Network (RNN). The CLL activation function was employed to improve the performance of the proposed DR classifier. The neuron's learning efficiency was significantly enhanced by the CLL activation, thus resulting in dominant outcomes. The proposed TCLLKEN obtained an accuracy of 98.99%, precision of 98.99%, recall of 98.98%, f-measure of 98.99%, and specificity of 98.97%. Likewise, the traditional EN attained 96.42738% accuracy, 96.488453% precision, 96.58393% recall, 96.84022% f-measure, and 96.89533% specificity. Here, because of the improper neuron activation, the traditional classifiers had poor DR prediction outcomes. Therefore, according to the experimental analysis, the proposed approach had high robustness in multi-grade DR outcomes.

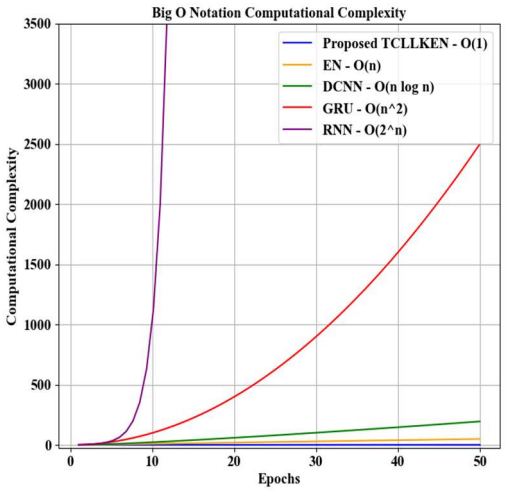

Figure 4: Complexity analysis

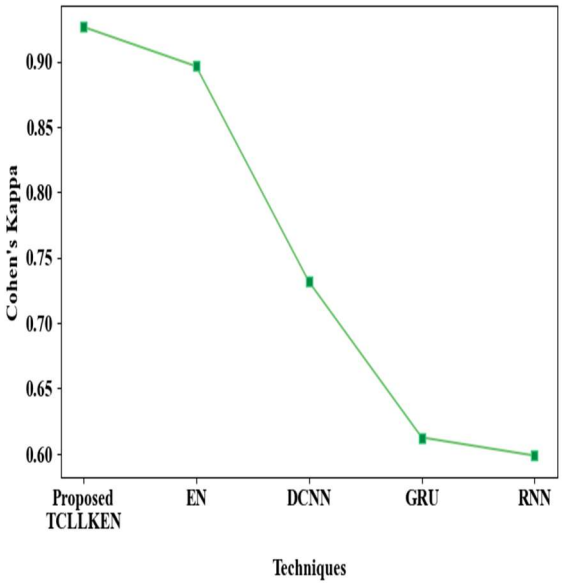

Figure 5: Cohen's Kappa Evaluation

Figures 4 and 5 depict the performance evaluation for multi-grade DR classification concerning the complexity and Cohen's kappa. Cohen's kappa of 0.9266 was attained by the proposed TCLLKEN, while a mean Cohen's kappa of 0.7098 was achieved by the conventional classifiers. As the number of epochs increased, the proposed model stabilized and reduced complexity. Nevertheless, the conventional classifiers had an abrupt spike in complexity, exhibiting instability. Here, owing to the absence of effective weight regularization, the conventional approaches had gradient instability

issues. The proposed work attained impressive performance by regularizing the suitable weights using the KPE, demonstrating its efficacy.

Table 5: Qualitative Analysis Of The Proposed TCLLKEN

Algorithms	Misclassification rate (%)	FPR	FNR
Proposed TCLLKEN	1.1	0.45	0.56
EN	1.5	0.7	0.8
DCNN	2.1	1.11	1.13
GRU	2.5	1.32	1.28
RNN	3.5	1.58	1.42

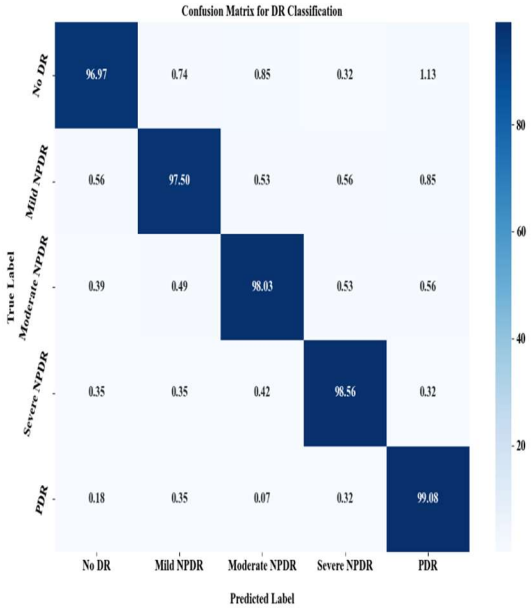

Figure 6: Confusion Matrix

The performance of the proposed TCLLKEN and existing algorithms regarding misclassification rate, False Positive Rate (FPR), and False Negative Rate (FNR) is validated in Table 5 and Figure 6. The proportion of incorrect predictions made by a classification model out of all predictions is referred to as the misclassification rate. The proportion of negative instances that are incorrectly classified as positive is measured by FPR. Similarly, the proportion of positive instances that are incorrectly classified as negative is measured by FNR. The dominant approach refers to the model with the minimum misclassification rate, FPR, and FNR. Here, the proposed TCLLKEN obtained a misclassification rate of 1.1, FPR of 0.45, and FNR of 0.56. However, the conventional RNN achieved a misclassification rate of 3.5, FPR of 1.58, and FNR of 1.42. Furthermore, a confusion matrix was utilized for validating the classifier's efficiency by contrasting the predicted labels with the actual labels. Therefore, the confusion matrix exhibited that DR was correctly classified by the proposed work with minimum errors. The presence of VLC analysis helped to capture the subtle vascular changes, thus leading to accurate DR grading outcomes. Nevertheless, owing to the lack of VLC factors, the existing methods had poor performance. In addition, to optimize the classifier's learning efficiency, the proposed work integrated TL and CLL activation, thereby reducing the misclassification rate. Hence, as per the empirical analysis, the proposed approach had better reliability in DR classification when contrasted with the conventional methods.

Table 6: Statistical Analysis For DR Classification

Metrics	TCLLKEN vs EN	TCLLKEN vs DCNN	TCLLKEN vs GRU	TCLLKEN vs RNN	Statistical significance
Accuracy	0.0001	0.0002	0.0005	0.0008	($p < 0.05$)
Precision	0.0003	0.0003	0.0008	0.0011	($p < 0.05$)
Recall	0.0004	0.0004	0.0009	0.0014	($p < 0.05$)
F-measure	0.0005	0.0005	0.0011	0.0016	($p < 0.05$)

Table 6 depicts the statistical analysis of the proposed TCLLKEN and prevailing classifiers like EN, DCNN, GRU, and RNN concerning the DR classification. To depict the efficiency of the proposed approach, the P-value analysis rendered a statistical evaluation. When compared with the proposed technique, the conventional algorithms had a limited statistical significance because of the improper weight regularization. The presence of the KPE in the proposed work helped to effectively tune the weight parameter. Furthermore, the learning efficiency of the proposed classifier was increased by the CLL activation. Hence, the proposed TCLLKEN attained a p-value less than 0.05. Therefore, the statistical significance validation showed that statistically significant improvements in performance metrics were ensured by the proposed TCLLKEN.

4.2.3 empirical assessment for vessel segmentation

Here, regarding vessel segmentation, the proposed FDMF's efficacy is investigated by comparing it with conventional methodologies, such as FF, Matched Filtering (MTF), Gabor Filters (GF), and Morphological Operators (MO).

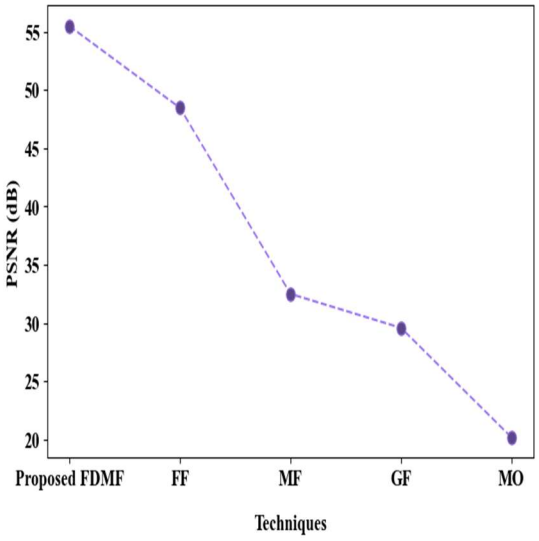

Figure 7: Performance Analysis Of The Proposed FDMF And Existing Techniques

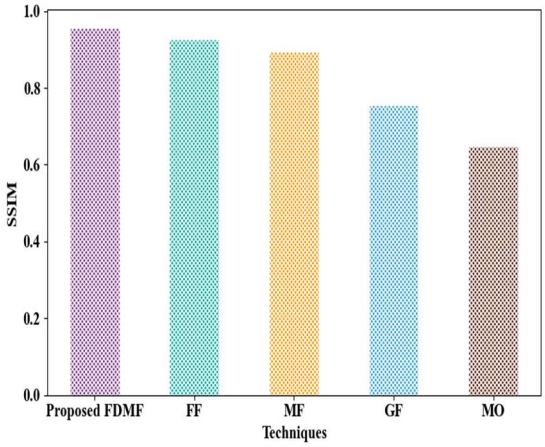

Figure 8: SSIM Analysis

In Figures 7 and 8, the performance analysis is done to depict the efficiency of the proposed FDMF in vessel segmentation. To validate the proposed work's performance, the quality metrics like Peak Signal-to-Noise Ratio (PSNR) and Structured Similarity Index Measure (SSIM) are considered. The model with maximum PSNR and SSIM is termed the superior approach. Therefore, the proposed FDMF attained a PSNR of 55.48 dB and an SSIM of 0.956. Contrarily, the traditional FF had PSNR and SSIM of 48.47 dB and 0.927, respectively, exhibiting poor performance. Owing to inadequate effective optical scale selection, the existing approaches were less effective. The inclusion of DMF in the proposed work helped to select the optimal scale range, thus leading to superior performance. So, when compared with the conventional schemes, the proposed work had higher significance in vessel segmentation.

4.2.4 Performance evaluation for region grouping

Likewise, concerning the quality metrics like clustering time, silhouette score, and dice coefficient, the numerical investigation for region grouping is done.

Table 7: Experimental Assessment For Region Grouping

Techniques	Clustering time (ms)	Silhouette score	Dice coefficient
Proposed DPBSPCA	2782	0.9894	0.9832

N			
DBSCAN	4898	0.8492	0.8785
K-means	6114	0.7492	0.6533
FCM	8678	0.6293	0.5294
CLARA	11048	0.5183	0.4923

In Table 7, the proposed DPBSPCAN's efficiency is assessed by comparing it with several existing algorithms like DBSCAN, K-means, FCM, and Clustering LARge Applications (CLARA). Here, the proposed DPBSPCAN attained a silhouette score of 0.9894 and a dice coefficient of 0.9832. On the contrary, the conventional DBSCAN obtained a silhouette score of 0.8492 and a dice coefficient of 0.8785. Subsequently, to perform clustering, the proposed DPBSPCAN and traditional CLARA consumed 2782ms and 11048ms, respectively. Due to the improper clustering parameter initialization, the existing methods had significant time complexity. Hence, high computational efficiency was achieved by the proposed work on account of the proper parameter initialization using PE and PDF.

4.2.5 Experimental analysis for resolution enhancement

The proposed DAFC-CLAHE's performance validation is displayed as follows,

Table 8: Comparative Validation For Resolution Enhancement

Approaches	MSE	RMSE	NMSE	MAE
Proposed DAFC-CLAHE	1.589	1.2605	0.019	1.672
CLAHE	3.679	1.918	0.031	2.233
HE	5.683	2.3839	0.046	3.471
DHE	8.289	2.879	0.062	4.291
GHE	10.921	3.3046	0.071	6.763

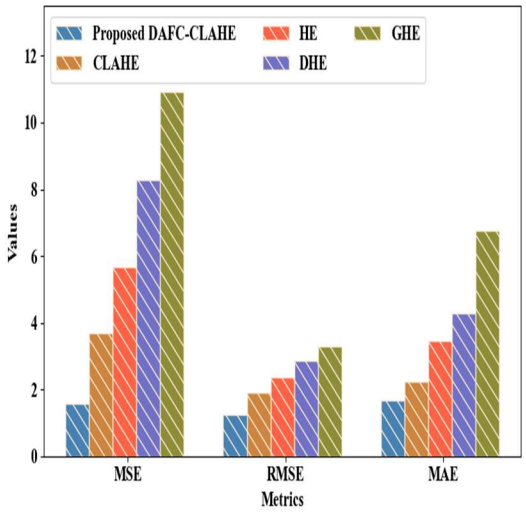

Figure 9: Performance assessment of the proposed DAFC-CLAHE

To prove the proposed model's prominence in resolution enhancement, the performance of the proposed DAFC-CLAHE and conventional techniques like CLAHE, Histogram Equalization (HE), Dynamic HE (DHE), and Global HE (GHE) is validated in Table 8 and Figure 9. The proposed DAFC-CLAHE obtained 1.589 MSE, 1.2605 Root MSE (RMSE), 0.019 Normalized MSE (NMSE), and 1.672 Mean Absolute Error (MAE). Nevertheless, due to the improper clip limit selection, the conventional techniques had a maximum error rate. Therefore, an impressive performance was acquired by the proposed work owing to the optimal clip limit selection using DAFC.

4.3 Comparative analysis of the proposed methodology

Here, the comparative assessment of the proposed approach and conventional works is performed to exhibit the model's efficiency in multi-grade DR classification.

Table 9: Comparative Analysis Of The Proposed Work

Author's name	Algorithm	Accuracy (%)	Precision (%)	F-measure (%)
Proposed work	TCLLKEN	98.99	98.99	98.99

(Hannan et al., 2025)	MobileNet V3-small, EN-b0, and DenseNet-169	80.00	82.00	82.10
(Mustafa et al., 2022)	MSDNN	85.46	90.00	91.00
(Wahab Sait, 2023)	HO-MobileNet v3	98.40	91.20	93.10
(Al-Antary & Arafa, 2021)	MSA-Net	84.60	-	98.20
(Ishtiaq et al., 2023)	Ensemble-optimized classifier	98.85	98.89	98.85
(Yang et al., 2024)	TMIL	85.6	-	-
(Elsharkawy et al., 2025)	FAETN	93.08	93.33	94.48
(Butt et al., 2025)	CNN	97.39	96.02	96.02
(Wang et al., 2025)	JFSPVT	90.7	91.4	90.8
(Thanikachalam et al., 2024)	Optimized deep CNN	97.91	97	-
(Balasamy & Suganyadevi, 2025)	Deep CNN	-	85.3	82.5

To prove the proposed model's prominence in multi-grade DR classification, the proposed work's performance is compared with several existing studies in Table 9. The proposed TCLLKEN obtained an accuracy of 98.99%, precision of 98.99%, and recall of 98.99%. To perform DR classification utilizing RFIs, the existing studies utilized techniques like CNN, Transformer model with Multiple Instance Learning (TMIL), Fused AutoEncoder Transformer Network (FAETN), Joint Frequency-Spatial Perception Vision Transformer (JFSPVT), MobileNetV3-small, EN-b0, DenseNet-169, Multi-Stream DNN (MSDNN), Hyperparameter-optimized MobileNet Version 3 (HO-MobileNet v3) model, Multi-Scale Attention Network (MSA-Net), and an ensemble-optimized classifier. Therefore, as per the analysis outcomes, the existing MSDNN attained 85.46% accuracy, 90.00% precision, and 91.00% f-measure (Mustafa et al., 2022). However, due to improper regularization, the existing work had limited performance. Further, the traditional ensemble-optimized classifier had accuracy, precision, and f-measure of 98.85%, 98.89%, and 98.85%, respectively (Ishtiaq et al., 2023). Similarly, the traditional CNN (Butt et al., 2025) obtained an accuracy of 97.39%, precision of 96.02%, and f-measure of 96.02%. Additionally, (Wang et al., 2025) utilized JFSPVT, which attained 90.7% accuracy, 91.4% precision, and 90.08% f-measure. Nevertheless, due to improper activation, the traditional classifiers were less effective. Here, the proposed work's performance was improved by using the CLL activation, which enhanced the classifier neurons' learning efficiency. Hence, in DR classification, the proposed work had better outcomes.

5. CONCLUSION

In this paper, a VLS-aware, accurate multi-grade DR classification approach was implemented using an improved TCLLKEN. The proposed work was generalized well enough to capture the VLS from the vessel graph. Thus, the significance of the DR staging was improved. The research technique included the objective innovations, including pre-processing, region grouping, vessel segmentation, vessel graph creation, VLS extraction, and DR classification. Thus, the proposed work's significant contributions are given as follows,

- The proposed DAFC-CLAHE was utilized to improve the FIs' resolution.
- To construct a vessel graph, the proposed work developed a novel MKST, capturing VLS like loop degree, area, and count.
- Additionally, GC extraction was employed in the proposed approach to effectively isolate the blood vessel structure.
- Furthermore, to highlight the subtle lesion characteristics and spatial features in the retinal images, the proposed work performed region grouping.

Eventually, several stages (No DR, mild NPDR, moderate NPDR, severe NPDR, and PDR) of the DR were effectively classified by the proposed

TCLLKEN with an accuracy of 98.98922%. Overall, in multi-grade DR classification, the proposed work obtained low complexity and maximum efficiency. Nevertheless, the proposed work mainly concentrated on retinal image-centric DR detection.

Clinical interpretability - Subtle vascular changes, which indicate the progression of DR, are highlighted by the VLS features, such as loop degree, loop area, and loop count. Clinicians can identify aberrant vessel growth by using loop degree, which depicts the branching patterns of vessels. Similarly, the loop area indicates limited vessel enlargement. Also, the density of vascular loops that mainly correlate with disease severity is revealed by the loop count. The above-mentioned vessel characteristics render interpretable markers that FIs can be effectively analyzed by the ophthalmologists to make reliable decisions.

Future scope: The future work will focus on incorporating the clinical data and multimodal imaging (Optical Coherence Tomography (OCT)) with RFIs during DR detection, thereby optimizing the model's robustness. In addition, federated learning techniques will be integrated in this approach to ensure data privacy while facilitating collaborative learning, ensuring generalizability in various clinical settings.

REFERENCES:

Dataset:

https://www.kaggle.com/datasets/ascanipek/eyepacs-aptos-messidor-diabetic-retinopathy

[1]. Abbood SH, Hamed HN, Rahim MS, Rehman A, Saba T, Bahaj SA. Hybrid retinal image enhancement algorithm for diabetic retinopathy diagnostic using deep learning model. IEEE Access. 2022 Jul 7;10:73079-86.

[2]. Priya SS. Detection and classification of diabetic retinopathy using pretrained deep neural networks. In2023 International Conference on Innovations in Engineering and Technology (ICIET) 2023 Jul 13 (pp. 1-7). IEEE.

[3]. Adriman R, Muchtar K, Maulina N. Performance evaluation of binary classification of diabetic retinopathy through deep learning techniques using texture feature. Procedia Computer Science. 2021 Jan 1;179:88-94.

[4]. Al-Antary MT, Arafa Y. Multi-scale attention network for diabetic retinopathy classification. IEEE Access. 2021 Apr 2;9:54190-200.

[5]. Ali G, Dastgir A, Iqbal MW, Anwar M, Faheem M. A hybrid convolutional neural network model for automatic diabetic retinopathy classification from fundus images. IEEE Journal of Translational Engineering in Health and Medicine. 2023 Jun 1;11:341-50.

[6]. Balasamy K, Suganyadevi S. Multi-dimensional fuzzy based diabetic retinopathy detection in retinal images through deep CNN method. Multimedia Tools and Applications. 2025 May;84(18):19625-45.

[7]. Bilal A, Sun G, Li Y, Mazhar S, Khan AQ. Diabetic retinopathy detection and classification using mixed models for a disease grading database. IEEe Access. 2021 Feb 1;9:23544-53.

[8]. Bilal A, Zhu L, Deng A, Lu H, Wu N. AI-based automatic detection and classification of diabetic retinopathy using U-Net and deep learning. Symmetry, 14 (7): 1427 [Internet]. 2022

[9]. Butt M, Awang Iskandar DN, Khan MA, Latif G, Bashar A. MEDCnet: A Memory Efficient Approach for Processing High-Resolution Fundus Images for Diabetic Retinopathy Classification Using CNN. International Journal of Imaging Systems and Technology. 2025 Mar;35(2):e70063.

[10]. Das D, Biswas SK, Bandyopadhyay S. A critical review on diagnosis of diabetic retinopathy using machine learning and deep learning. Multimedia Tools and Applications. 2022 Jul;81(18):25613-55.

[11]. Das S, Kharbanda K, Raman R, Dhas E. Deep learning architecture based on segmented fundus image features for classification of diabetic retinopathy. Biomedical Signal Processing and Control. 2021 Jul 1;68:102600.

[12]. Dayana AM, Emmanuel WS. An enhanced swarm optimization-based deep neural network for diabetic retinopathy classification in fundus images. Multimedia Tools and Applications. 2022 Jun;81(15):20611-42.

[13]. Dutta A, Agarwal P, Mittal A, Khandelwal S. Detecting grades of diabetic retinopathy by extraction of retinal lesions using digital fundus images. Research on Biomedical Engineering. 2021 Dec;37(4):641-56.

[14]. Elsharkawy M, Abdelhalim I, Mahmoud A, Gamal A, Abd-Elhady MS, Sewelam A, El-Baz A. Fused-AETNet: A variational transformer-based framework for diabetic retinopathy classification using OCT biomarkers. IEEE Access. 2025 Sep 11.
[15]. Hannan A, Mahmood Z, Qureshi R, Ali H. Enhancing diabetic retinopathy classification accuracy through dual-attention mechanism in deep learning. Computer Methods in Biomechanics and Biomedical Engineering: Imaging & Visualization. 2025 Dec 31;13(1):2539079.
[16]. Hayati M, Muchtar K, Maulina N, Syamsuddin I, Elwirehardja GN, Pardamean B. Impact of CLAHE-based image enhancement for diabetic retinopathy classification through deep learning. Procedia Computer Science. 2023 Jan 1;216:57-66.
[17]. Hu J, Wang H, Wang L, Lu Y. Graph adversarial transfer learning for diabetic retinopathy classification. IEEE Access. 2022 Nov 9;10:119071-83.
[18]. Ikram A, Imran A, Li J, Alzubaidi A, Fahim S, Yasin A, Fathi H. A systematic review on fundus image-based diabetic retinopathy detection and grading: Current status and future directions. IEEE Access. 2024 Jul 12.
[19]. Ishtiaq U, Abdullah ER, Ishtiaque Z. A hybrid technique for diabetic retinopathy detection based on ensemble-optimized CNN and texture features. Diagnostics. 2023 May 22;13(10):1816.
[20]. Kalyani G, Janakiramaiah B, Karuna A, Prasad LN. Diabetic retinopathy detection and classification using capsule networks. Complex & Intelligent Systems. 2023 Jun;9(3):2651-64.
[21]. Meruva SK, Tulasi VG, Vinnakota N, Bhavana V. Risk Level Prediction of Diabetic Retinopathy based on Retinal Images using Deep Learning Algorithm. Procedia Computer Science. 2022 Jan 1;215:722-30.
[22]. Mustafa H, Ali SF, Bilal M, Hanif MS. Multi-stream deep neural network for diabetic retinopathy severity classification under a boosting framework. IEEE Access. 2022 Oct 26;10:113172-83.
[23]. Özbay E. An active deep learning method for diabetic retinopathy detection in segmented fundus images using artificial bee colony algorithm. Artificial Intelligence Review. 2023 Apr;56(4):3291-318.
[24]. Qureshi I, Ma J, Abbas Q. Diabetic retinopathy detection and stage classification in eye fundus images using active deep learning. Multimedia Tools and Applications. 2021 Mar;80(8):11691-721.
[25]. Rachapudi V, Rao KS, Rao TS, Dileep P, Deepika Roy TL. Diabetic retinopathy detection by optimized deep learning model. Multimedia Tools and Applications. 2023 Jul;82(18):27949-71.
[26]. Romero-Oraá R, Herrero-Tudela M, López MI, Hornero R, García M. Attention-based deep learning framework for automatic fundus image processing to aid in diabetic retinopathy grading. Computer Methods and Programs in Biomedicine. 2024 Jun 1;249:108160.
[27]. Sangeetha K, Valarmathi K, Kalaichelvi T, Subburaj S. A broad study of machine learning and deep learning techniques for diabetic retinopathy based on feature extraction, detection and classification. Measurement: Sensors. 2023 Dec 1;30:100951.
[28]. Sawant J, Vibhute AD. U-Net-based blood vessel segmentation using an improved data augmentation with green channel images. Procedia Computer Science. 2025 Jan 1;260:1071-9.
[29]. Singh SP, Gupta P, Dung R. Diabetic retinopathy detection by fundus images using fine tuned deep learning model. Multimedia Tools and Applications. 2024 Nov;83(39):86657-79.
[30]. Thanikachalam V, Kabilan K, Erramchetty SK. Optimized deep CNN for detection and classification of diabetic retinopathy and diabetic macular edema. BMC Medical Imaging. 2024 Aug 28;24(1):227.
[31]. Uppamma P, Bhattacharya S. Deep learning and medical image processing techniques for diabetic retinopathy: a survey of applications, challenges, and future trends. Journal of HealthcareEngineering.2023;2023(1):2728719 .
[32]. Usman TM, Saheed YK, Ignace D, Nsang A. Diabetic retinopathy detection using principal component analysis multi-label feature extraction and classification. International Journal of Cognitive Computing in Engineering. 2023 Jun 1;4:78-88.
[33]. Wahab Sait AR. A lightweight diabetic retinopathy detection model using a deep-learning technique. Diagnostics. 2023 Oct 3;13(19):3120.
[34]. Wang Y, Shen S, Tong N. JFSP-ViT: A Joint Frequency-Spatial Perception Vision

ISSN: 1992-8645 www.jatit.org E-ISSN: 1817-3195

Transformer for Diabetic Retinopathy Grading. IEEE Access. 2025 Aug 19.

[35]. Xu X, Liu D, Huang G, Wang M, Lei M, Jia Y. Computer aided diagnosis of diabetic retinopathy based on multi-view joint learning. Computers in Biology and Medicine. 2024 May 1;174:108428.

[36]. Yang Y, Cai Z, Qiu S, Xu P. A novel transformer model with multiple instance learning for diabetic retinopathy classification. IEEe Access. 2024 Jan 8;12:6768-76.